Parasitic Currents in Stray Paths of Some Topologies of YASA AFPM Machines: Trend with Machine Size

A. Di Gerlando, *Member*, IEEE, G. M. Foglia, M. F. Iacchetti, *Member*, IEEE, R. Perini, *Member*, IEEE

***Abstract*— In some topologies of YASA (Yokeless And Segmented Armature) AFPM (Axial Flux Permanent Magnet) Machines, the particular frame structure required to fasten floating teeth can originate stray paths where parasitic currents may circulate. The paper investigates how the amplitude of these currents and the related additional Joule losses depend on the machine size. Reference is made to wind energy generators, rated from some tens of kWs up to a few MWs. The developed model is mainly based on wind turbine basic data of vendor data sheets, and on the quantities evaluated and tested in two YASA AFPM prototypes, rated 50 and 200 kW.**

***Index Terms* – PM machines, Axial Flux Machines, Yokeless And Segmented Armature Machines, Parasitic Current Paths due to Fixing Frame Structure.**

NOMENCLATURE

A_c cross section area of the cylindrical spacers;
A_g annular air gap cross section area;
A_t tooth section area;
b_{ray} ray breadth;
b_{rim} rim breadth;
b_{slot} slot width
B_m no–load working value of the PM flux density;
B_r PM residual flux density;
B_t tooth flux density;
d_r ray deflection: $d_r = k_{dr} \cdot g_n$;
D_i AFPM machine core internal diameter;
D_e AFPM machine core external diameter;
D_t turbine rotor diameter;
E Young modulus;
$E_{A.k}$ EMF of the k-th loop A;
$E_{B.k}$ EMF of the k-th loop B;
E_n no-load line-to-line EMF;
$E_{p\ell h}$ rms value of the parasitic loop EMF h-th harmonic;
f_n rated frequency;
f_0 reference frequency at a reference turbine power P_0;
F total mechanical load acting on one ray;
F_{ax} resultant axial force between stator and rotor, due to a variation Δg of the air gap;
F_{ref} reference resultant axial force produced in one air-gap;
g_e equivalent magnetic air gap = $g_n + h_m / \mu_{rpu}$;
g_n rated air gap width;
h_m PM axial length;
$I_{A.k}$ current of the k-th loop A;
$I_{B.k}$ current of the k-th loop B;
$I_{cyl.1}$ rms of the fundamental current flowing in one outer cylindrical spacer;
$I_{loop.1}$ rms of the fundamental current flowing in one loop;
I_n rated current;
$I_{ray.1}$ rms of the fundamental current flowing in one ray;
J moment of inertia of a ray = $b_{ray} \cdot t_r^{\,3}/12$
ℓ_{ax} axial length of the AFPM machine;
ℓ_m radial size of PMs;
ℓ_{ce} lengths of the external cylindrical spacers;
ℓ_{ci} lengths of the internal cylindrical spacers;
$L_{p\ell}$ inductance of the parasitic loop;
ℓ_{ray} ray length;
ℓ_{rim} rim length;
k_D AFPM diameter ratio: $k_D = D_i / D_e$;
k_{dr} proportionality coefficient: $d_r = k_{dr} \cdot g_n$;
k_g proportionality coefficient: $g_n = k_g \cdot D_e$;
k_m proportionality coefficient: $h_m = k_m \cdot g_n$;
k_{th} harmonic composition factor of 2 nearby teeth fluxes;
x pu synchronous reactance of the AFPM machine;
N_n rated rotational speed [rpm];
N_t No of teeth per module;
N_c No of Geometric Cycles (GCs) per module;
N_{tc} No of teeth per GC = No of coils per GC = N_t / N_c;
N_{tcph} No of teeth per GC per phase = No of coils in one GC per phase; for a 3-phase machine: $N_{tcph} = N_t /(3 \cdot N_c)$;
p No of poles (No of PMs on each rotor disk face);
p_c No of poles per GC = No of PMs per GC = p / N_c ;
P_n AFPM machine rated power [kW];
$P_{loss.1}$ Joule losses due to first harmonics of parasitic currents;
P_t turbine rated power [kW];
q uniformly distributed force on the ray = F/ ℓ_{ray};
R_{ce} resistance of one external spacer;
R_{ci} resistance of one internal spacer;
R_{ray} resistance of one ray;
R_{rim} resistance of the rim portion between two rays;
t_r ray and rim thickness;
$X_{p\ell n}$ parasitic loop reactance at the rated frequency;
V_n Line-to-line rated voltage;
α_e slot angle = $(2\pi/N_t) \cdot (p/2)$;
α_m p.u. peripheral extension of each PM, ratio between PM width and pole pitch;
$\varphi_{m.tot}$ absolute value of the total PM flux, equal to the flux of one PM multiplied by the No of poles;
φ_t tooth flux;
$\varphi_{t.tot}$ absolute value of the total teeth flux;
Φ_{tp} no-load peak value of the tooth flux, occurring in the tooth-axis PM-axis alignment condition;

Manuscript received June 29, 2015; revised October 9, 2015; accepted November 18, 2015.

A. Di Gerlando, G.M. Foglia, R. Perini are with the Department of Energy, Politecnico di Milano, Via Lambruschini 4, 20156 Milano, Italy. M.F. Iacchetti is with the School of Electrical and Electronic Engineering, University of Manchester, Sackville Street Building, Manchester, M13 9PL, UK. e-mails: roberto.perini@polimi.it ; gianmaria.foglia@polimi.it ; matteo.iacchetti@manchester.ac.uk ; antonino.digerlando@polimi.it

Φ_{th} h-th harmonic of the tooth flux;
μ_{rpu} PM p.u. recoil permeability
η AFPM machine efficiency;
ρ_s steel resistivity = $1.5 \cdot 10^{-6}$ [Ω·m];
ω_n rated angular frequency = $2\pi f_n$;
ω_h angular frequency of h-th harmonic $\omega_h = h\ \omega_n$.

I. Introduction

AXIAL Flux Permanent Magnet (AFPM) Machines are usually renowned as characterized by greater torque density than radial flux machine configurations [1]. Besides, since a large number of pole pairs can be adopted, AFPM machines are suited for direct drive applications, at low speed, high torque operating conditions, as electro-mechanical propulsion systems, in-wheel motors, elevators, wind energy generators [2]-[9].

Various AFPM arrangements have been developed [1], [10]-[12]. If a stator core exists, two dispositions can be employed: single-stator double-rotor AFPM machines, i.e. Torus machines, or double-stator single-rotor AFPM machines, i.e. Kaman machines [13].

Frequently the core consists of a rolled laminated cylinder (in such a way that the stacking direction results the radial one). In fact, a core consisting of a laminated ring with axial stacking direction would result stiffer, but at the price of an increase in eddy current losses [14]. If no slots are needed in the laminated cylinder, its manufacture is greatly simplified, as slots would call for punching the iron tape with non-uniform pitch.

To avoid such an issue, an alternative arrangement for Torus kind machines is the so called YASA (Yokeless And Segmented Armature) configuration [15]. As the name indicates, no yoke exists in the core, and the teeth are magnetically independent: thus, the lamination stack is much easier to be manufactured. The YASA layout gives many benefits [16], among which: (a) short end windings and reduced Joule losses, (b) simpler winding assembly and high winding fill factor, (c) very low inductive coupling among phases, with improved fault tolerance capability, (d) minimized winding and core mass.

However, the YASA disposition leads to two further issues. The first one is due to the inherently tapered profile of teeth, demanding variable-width lamination punching. Some manufacturing techniques have been proposed in order to simplify the punching process, such as: milling pre-assembled parallelepiped lamination stacks [17] or staking alternately-displaced laminations having the same punched profile [18]. An interesting investigation and comparison among several lamination stacking methods is performed in [19]. The second challenge is providing an adequate frame structure to the teeth. In some stator structures, teeth are embedded into a composite-material ring [20], which also houses shaped cooling ducts. Such a solution is also used with SMC teeth [15], [21], [22]. Further arrangements to position and fasten stator teeth rely to radial tie-rods [23] or retentive rings [16]. The former solution can lead to imperfect stator construction [23], whereas the latter seems to be the solution adopted in some patents, [24]-[25], which are used also in commercial YASA motors [26]. In another solution, the central zone of the teeth is unwound, so they can be inserted in a bulk retaining disk [27]. However, all the aforementioned solutions can be used just in case of medium-low rating machines.

For medium-high rating machines, an alternative stator structure consists of hollow and rayed plate pairs assembled with spacers and pre-tensioned tie rods to provide adequate stiffness. As detailed in Fig. 1, each tooth is fastened between contiguous rays. This disposition has been adopted for two prototypes of a three phase AFPM synchronous machine (SM) (Fig. 1c and Figs. 2, 3), both employed as wind energy generators. Figs. 2, 3 show a picture of the machines, while Tables I, II resume their main data (see also [18], [28], [29]).

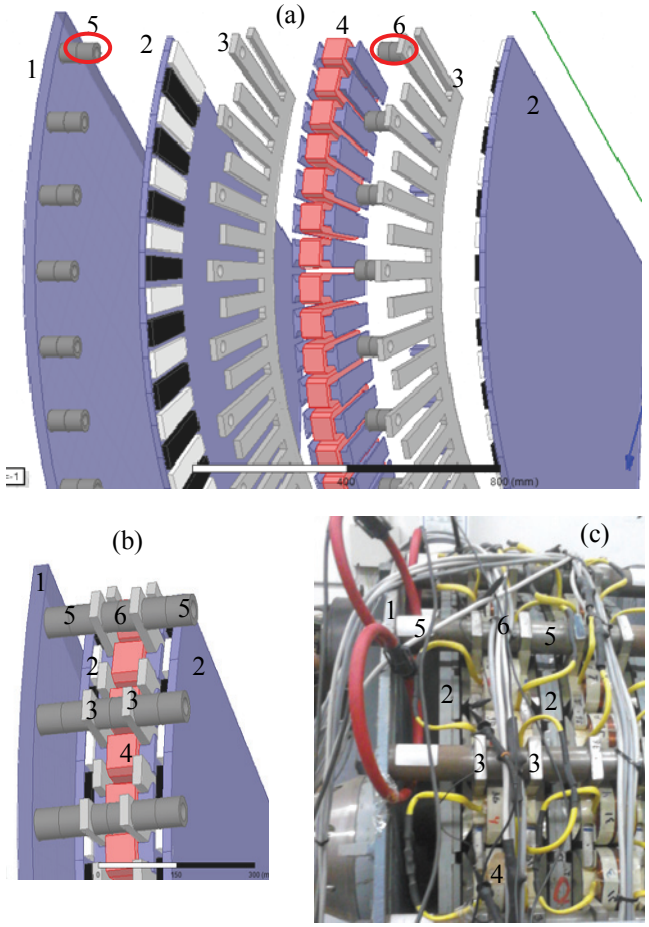

Fig. 1. Exploded (a) and compact (b) views of one sector of half of the YASA AFPM prototype (c) whose fixing structure uses rays and tie-rods. 1: stator plate; 2: rotor disks with PMs; 3: ray structures; 4: wound teeth; 5, 6: outer and inner spacers respectively, in which tie-rods are threaded.

Unfortunately, the overall frame structure inherently creates parasitic loops through tie-rods, rays, and plates, in which electro-motive forces (EMFs) are induced during the PM rotor rotation. Even if the induced parasitic EMFs have very low amplitudes, the parasitic loops impedance is very low too, thus the parasitic currents may easily reach hundreds of amperes. Preventing the parasitic current circulation is technically challenging and costly, due to the narrow mechanical tolerances to be guaranteed in the machine construction. Insulations between contact surfaces of spacers and plates require high-stiffness, dimensionally-stable and corrosion-proof materials and careful assembly procedures as well.

The genesis mechanism of parasitic currents in the frame structure has been studied [30], [31], and a model for predicting parasitic currents has been developed and

validated by some measurements on prototypes. However, no discussion and calculations of the additional Joule losses produced by parasitic currents have been provided in [30] and [31]. In addition, [30] and [31] do not analyze the impact of the scale effects on parasitic currents and related losses. Nevertheless, the full understanding of the scale effects is crucial for the proper design of high-rating YASA AFPM machines. This paper addresses all these pending issues by investigating the dependence of the parasitic current amplitude on the machine size and discussing the impact on additional Joule losses. The outcomes of such investigations provide the basis to evaluate the advisability of insulating layers at the contact interfaces between spacers and rays or plates, depending on the scale effects. To this purpose, the parameters of the parasitic path branches and the machine construction and operation quantities are preliminarily expressed as a function of the rated power, by invoking general sizing criteria and rather usual characteristic aspect ratios extrapolated from existing machine designs. They include two constructed prototypes of different scale (50 kW / 70 rpm and 200 kW / 35 rpm) and the design of a third machine (2MW/17 rpm, Table III).

All the predictions regarding the amplitude of the parasitic currents and the related additional Joule losses are compared with the measurements on the two prototypes. In order to obtain experimental evidence of the parasitic currents and the related additional Joule losses, the two considered prototypes have been purposely built without any frame insulation.

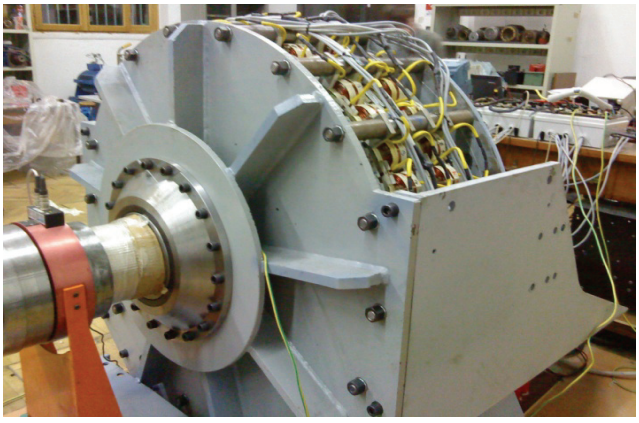

Fig. 2. Photograph of the 50 kW / 70 rpm three phase AFPMSG prototype.

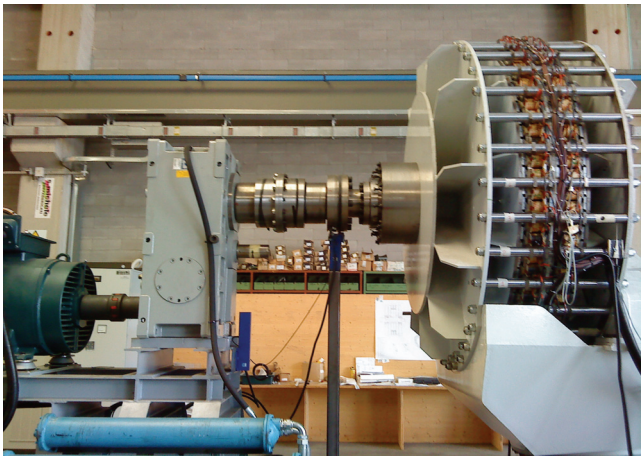

Fig. 3. Photograph of the 200kW / 35rpm three phase AFPMSG prototype.

The paper is structured as follows. Sec. II resumes the genesis of the parasitic currents. Sec. III reports the results of a survey among the commercial turbine data sheets, to gain a relation between the turbine power and both the turbine speed and the maximum generator external diameter. Based on the two prototypes, Sec. IV investigates the relation between the power and the main electro-mechanical quantities of the generator (air gap, poles number, cycle number, teeth number). In Sec. V, the geometrical sizes involved in the evaluation of the resistances of the parasitic paths are expressed as a function of the power: this way, the reactance and the resistances can be evaluated as a function of the machine power. In Sec. VI a single-loop simplified model is developed, to quickly estimate the rms value of the parasitic current. Finally, in Sec. VII the parasitic EMFs and currents are evaluated by means of the model, and compared with the values measured on the prototypes.

TABLE I
MAIN DESIGN DATA OF THE 50 KW/70 RPM 3-PHASE AFPMSG PROTOTYPE

Line-to-line rated Voltage V_n ,no-load e.m.f. E_n [V]	625, 750
Rating P_n [kW], speed N_n [rpm], frequency f_n [Hz]	50, 70, 22.17
Rated current I_n [A], eff. η [%], reactance x [pu]	46.3, 92.6, 0.50
Pole No = PM No p, teeth No N_t	38, 36
Cycle No N_c, teeth/cycle/phase N_{tcph} , pole/cycle p_c	2, 6, 19
Ext. diam. D_e , int. diam. D_i , axial length ℓ_{ax} [mm]	1100, 914, 330

TABLE II
MAIN DESIGN DATA OF THE 200 KW/35 RPM 3-PHASE AFPMSG PROTOTYPE

Line-to-line rated Voltage V_n ,no-load e.m.f. E_n [V]	624, 718
Rating P_n [kW], speed N_n [rpm], frequency f_n [Hz]	200, 35, 22.75
Rated current I_n [A], eff. η [%], reactance x [pu]	185, 93.3, 0.34
Pole No = PM No p, teeth No N_t	78, 72
Cycle No N_c, teeth/cycle/phase N_{tcph} , pole/cycle p_c	6, 4, 13
Ext. diam. D_e , int. diam. D_i , axial length ℓ_{ax} [mm]	2100, 1680, 376

TABLE III
MAIN DESIGN DATA OF THE 2 MW/17 RPM 3-PHASE AFPMSG DESIGN

Line-to-line rated Voltage V_n ,no-load e.m.f. E_n [V]	624, 828
Rating P_n [kW], speed N_n [rpm], frequency f_n [Hz]	2000, 17, 14.73
Rated current I_n [A], eff. η [%], reactance x [pu]	1851, 94.3, 0.59
Pole No = PM No p, teeth No N_t	104, 96
Cycle No N_c, teeth/cycle/phase N_{tcph} , pole/cycle p_c	8, 4, 13
Ext. diam. D_e , int. diam. D_i , axial length ℓ_{ax} [mm]	5000, 3600, 589

II. GENESIS OF THE PARASITIC CURRENTS

Fig. 1a shows that the ray structure is made by the rays and by an internal rim which connects them; the same figure shows that long and short rays are alternatively disposed. Only long rays are connected by tie-rods, whereas short rays are floating. Two consecutive long rays, together with the portion of internal rim between them, form an open loop, which is closed by the tie-rods and the stator plate (Fig. 4). Such parasitic loops embrace two teeth, thus they link the resultant flux of two adjacent teeth.
In no-load operation, fluxes in adjacent teeth are almost opposite each other, because the tooth pitch is close to the PM pitch; however, the resultant flux is not zero. Due to the PM rotation, this parasitic loop flux linkage is alternate: therefore it induces EMFs in the loops.

In the following, the analysis is developed just considering the machine no-load operation. This is well suited to correctly predict parasitic currents; in fact:
– most parasitic loops (sometimes all of them, depending on the winding layout) embrace two coils belonging to the

same phase: however, due to their reverse series connection, even in loaded operation the armature reaction MMF acting in each loop has a zero resultant;
– for the few parasitic loops whose embraced coils belong to different phases, the resultant MMF amplitude equals that of one coil, due to a 120 deg phase displacement;
– in loaded rated conditions, the coil MMF amplitude is roughly 1/10 of the equivalent PM MMF.

The soundness of this approach has been confirmed by some tests, which showed that parasitic currents and related losses do not significantly increase in load operation compared with no load operation.

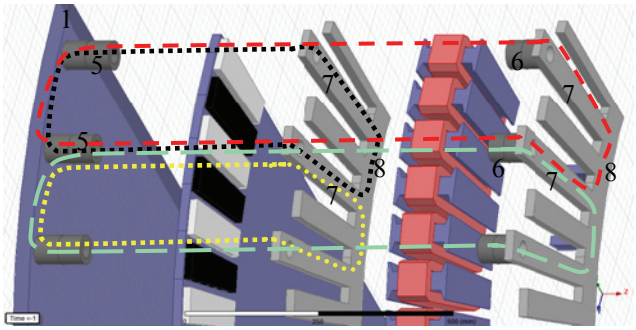

Fig. 4. Parasitic loops, formed by: two long rays (7), portion of internal rim between them (8), spacers (5 outer, or 6 inner), stator plate (1).

III. Speed and Diameter Versus Machine Rating

Based on the available turbine data sheets, a survey has been performed to gain the trend of both the turbine rated speed N_n and the turbine rotor diameter D_t versus the turbine power P_t .

Figs. 5a-5b show the found data points, together with the adopted fitting equations:

$$N_t(P_t) = 213.79\cdot(P_t[\text{kW}])^{-0.326} \ \text{[rpm]}$$
$$D_t(P_t) = 3.383\cdot(P_t[\text{kW}])^{0.4213} \ \text{[m]} \qquad (1)$$

Starting from the turbine diameter, and by adopting suited reduction coefficients, the AFPM generator external diameter D_e can be estimated, as a function of the power.
In particular, on the basis of the average manufacturers' data, the nacelle diameter has been assumed 7.5% of D_t, and D_e equal to 80 % of the nacelle diameter, therefore:

$$D_e(P_t) = 0.06\cdot D_t(P_t[\text{kW}]) \quad \text{[m]}. \qquad (2)$$

In Fig. 5c, the fitting curves $N_t(P_t)$ and $D_e(P_t)$ by (1) and (2) are shown, together with the corresponding points for the power rating values P_t = 50, 200, 2000 kW. Solid markers (■ and ▲, respectively for N_n and D_e) represent the actual values of the prototypes (50, 200 kW), while the empty markers (□, Δ) refer to the corresponding values of a design for a 2 MW machine. It can be seen that the values fairly agree with the fitting equations trend.

IV. Main Electro-Mechanical Quantities Versus Machine Rating

Based on the sizes of the two prototypes, the relation among the machine power rating P_t and the main electro-mechanical quantities is investigated.

First of all, the following proportionality laws are assumed: air gap $g_n \propto D_e$; PM axial width $h_m \propto g_n$:

$$g_n(P_t)\ [\text{mm}] = k_g\cdot(D_e(P_t)\ [\text{m}]), \quad k_g = 2\ [\text{mm/m}]$$
$$h_m(P_t)\ [\text{mm}] = k_m\cdot g_n(P_t), \quad k_m = 3 \qquad (3)$$

The rated generator frequency f_n is assumed dependent on P_t on the basis of the relation

$$f_n(P_t) = f_0\cdot\exp(-P_t/P_0) \qquad (4)$$

where f_0 = 23.0 Hz, P_0 = 4686 kW; such values allow to fairly fit the prototype data (f_n in Tables I and II) together with a plausible frequency value for a high rated designed generator (15 Hz @ 2 MW).

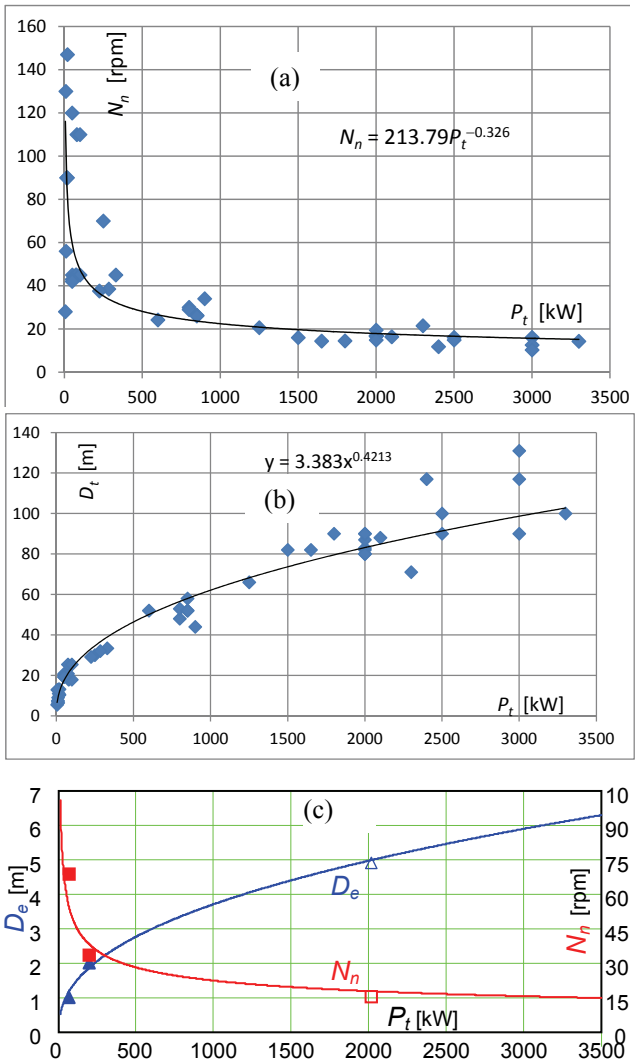

Fig. 5. Curves as a function of the rated turbine power P_t [kW]:
(a) top: turbine rated speed N_n [rpm] as a function of P_t (vendors' data);
(b) middle: turbine diameter D_t [m] as a function of P_t (vendors' data);
(c) bottom: fitting equations of the turbine rated speed N_n and of the AFPM machine external diameter D_e [m] as a function of P_t ; the points give the corresponding actual values of constructed prototypes (full points: P_t = 50, 200 kW) and of a designed machine (empty marker: P_t = 2 MW).

According to the generator operation principle ([18],[28]), one of the most important machine characteristic is the number of tooth coils per cycle per phase N_{tcph} (i.e.: the number of series connected coils in one cycle, belonging to one phase). It does not depend on the machine size, but it is related to the electromagnetic operation: its meaning is similar to the number of slot/pole/phase in distributed winding machine (the higher N_{tcph} , the lower the EMF waveform distortion).

N_{tcph} is preferably an even number, and its most common values are 4 or 6; in fact, the 50 kW and 200 kW prototypes adopt N_{tcph} = 6 and 4 respectively. In the following, N_{tcph} will be assumed as a parameter for the generator design, and both cases (N_{tcph} = 4; 6) will be considered.

Based on the design procedure ([18], [28]), the generator pole number p, cycle number N_c and teeth number N_t, can be expressed as a function of f_n and P_t, with N_{tcph} as parameter:

$$\begin{aligned} p(f_n,P_t) &= Round\left(\frac{120\cdot f_n}{N_n(P_t)},2\right) \\ N_c(f_n,P_t,N_{tcph}) &= Round\left(\frac{p(f_n,P_t)}{3\cdot N_{tcph}+1},1\right) \\ N_t(f_n,P_t,N_{tcph}) &= p(f_n,P_t)-N_c(f_n,P_t,N_{tcph}) \end{aligned} \quad (5)$$

where the function *Round*(x, y) rounds the number x as the nearest multiple of y.
By substituting (4) in (5), the dependence on f_n disappears, and the quantities depend only on the power P_t (and on the parameter N_{tcph}).

V. Geometrical Sizes Involved in the Parasitic Paths Resistances and Reactance

Fig. 4 shows that four branches are involved in the parasitic loops: the long rays (element number 7), the portion of internal rim between them (8), the cylindrical spacers (5 outer, 6 inner). Fig. 6 shows these four elements and their geometrical dimensions, which are needed for the evaluation of the parasitic paths resistances: lengths of the external and internal cylindrical spacers (ℓ_{ce}, ℓ_{ci}) and their section area (A_c), ray and rim length, breadth, thickness (ℓ_{ray}, ℓ_{rim}, b_{ray}, b_{rim}, t_r).

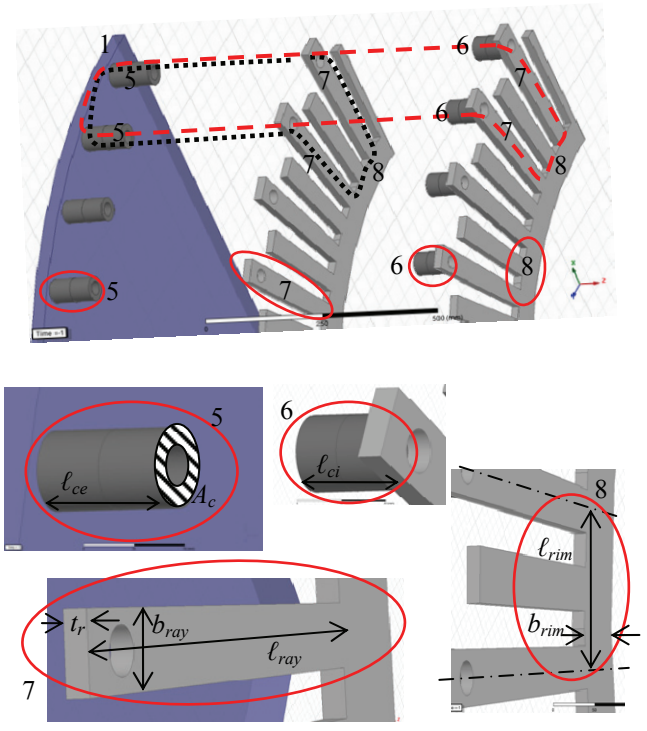

Fig. 6. Top: branches involved in the parasitic loops: the long rays (element number 7), the portion of internal rim between them (8), the cylindrical spacers (5 outer, 6 inner). Bottom: geometrical dimensions of the four elements 5, 6, 7, 8.

In the following, all these dimensions are expressed as a function of the machine power. The stator plate (element 1 in Fig.s 4 and 6) is not considered, since it offers a negligible resistance to the parasitic currents, compared with the resistances of the other involved branches.

A. Radial size ℓ_m of PMs and teeth.

The Radial size ℓ_m can be expressed as

$$\ell_m(P_t) = (1-k_D)\cdot D_e(P_t)/2 \quad , \quad (6)$$

where k_D = D_i / D_e, and D_i = AFPM generator internal diameter. On the basis of the values adopted for the two prototypes, in this analysis it is assumed k_D = 0.75.

B. Ray width b_{ray}.

The annular air gap section area A_g can be expressed as

$$A_g = \frac{\pi}{4}D_e^2\left(1-k_D^2\right) \quad . \quad (7)$$

Let us indicate with α_m the p.u. peripheral extension of each PM (i.e.: the ratio between the PM width and the polar pitch), and with B_m the PM working value of the no–load flux density. The absolute value of the total PM flux $\varphi_{m.tot}$ (equal to the flux of one PM multiplied by the No of poles) can be obtained by multiplying A_g times α_m and B_m ; by neglecting the PM leakage flux, $\varphi_{m.tot}$ can be considered equal to the absolute value of the total teeth flux $\varphi_{t.tot}$; therefore, the flux φ_t of one tooth can be obtained by dividing $\varphi_{t.tot}$ by the teeth No N_t ; finally, by dividing φ_t by the tooth flux density B_t, the tooth section area A_t follows:

$$A_t = \frac{\pi}{4}D_e^2\left(1-k_D^2\right)\alpha_m B_m \frac{1}{N_t}\frac{1}{B_t} \quad . \quad (8)$$

The section area of one inter-teeth slot can be expressed as $A_g/N_t - A_t$, and dividing it by ℓ_m gives the slot width b_{slot}. Since the ray width b_{ray} equals the slot width, we obtain

$$b_{ray} = \frac{\pi}{4}D_e^2\left(1-k_D^2\right)\frac{1}{N_t}\left[1-\alpha_m\frac{B_m}{B_t}\right]\frac{1}{\ell_m} \quad (9)$$

By putting (6) in (9), we gain

$$b_{ray}(P_t,N_{tcph}) = \frac{\pi}{2}D_e(P_t)\cdot\left(1+k_D\right)\frac{1}{N_t(P_t,N_{tcph})}\left[1-\alpha_m\frac{B_m}{B_t}\right]. \quad (10)$$

According to the prototype design values, in this analysis it is assumed α_m = 0.8, B_m = 0.75 (T), B_t = 1.75 (T).

C. Ray and rim thickness t_r.

In an ideal AFPM machine, the distance between the rotor and the stator is the same all over the air gap, thus the net axial force between the stator and the rotor is zero; unfortunately, in actual machines, manufacturing imperfections always exist, therefore a resultant attraction force occurs between the stator teeth and the rotor disk. This force acts on each ray, which behaves as a fixed-end beam, and tends to bend, reducing the air gap, with a contact risk. A simplified static scheme for the evaluation of the ray deflection is provided in Fig. 7.

Being the two rims bolted together through an inner spacer array (not shown in Fig. 6), such an assembly is treated as a rigid body, suspended to the cylindrical spacers of the stator frame by rays. The additional flexibility inherently due to the rim plates is roughly accounted for by placing virtual hinges between rays and rims. Rigid stator

spacer and tie rod assemblies are assumed, as their bending stiffness is much higher than the ray one.

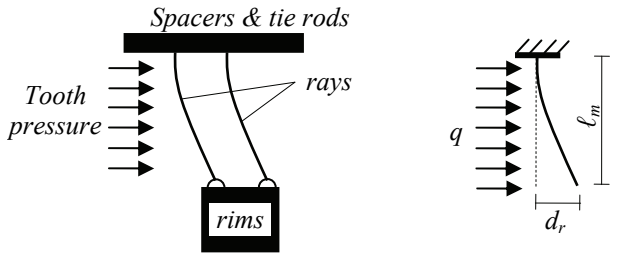

Fig. 7. Static scheme of the stator rim - ray and spacer assembly for the ray deflection estimation.

The ray thickness t_r must be high enough to limit the ray deflection d_r to a fraction k_{dr} of the rated air gap g_n (i.e.: $d_r = k_{dr} \cdot g_n$). By imposing a limit value of k_{dr} , the minimum t_r value can be obtained. In fact, the deflection d_r of the equivalent fixed-end beam under a uniformly distributed force q is expressed by

$$d_r = \frac{1}{8}\frac{q\ell_m^4}{EJ} \quad . \tag{11}$$

By rearranging (11) with $q=F/\ell_m$ and $J=b_{ray}\cdot t_r^3/12$, the thickness t_r is obtained:

$$t_r = \left\{\frac{3}{2E}\frac{F\cdot \ell_m^{\,3}}{(k_{dr}\cdot g_n)\cdot b_{ray}}\right\}^{\frac{1}{3}} \quad . \tag{12}$$

Since there are two spokes in parallel (spoke pair) which support two teeth and since there is one floating spoke pair every two, F is the force acting on a tooth. This can be expressed as F_{ax}/N_t , where F_{ax} is the resultant axial force acting between the stator and the rotor due to a variation Δg of the air gap ($+\Delta g$ in one side air gap and $-\Delta g$ in the other one). The variation Δg is assumed as caused by an axial displacement of the rotor disk, occurred during the assembling procedure. The study presented in [32] showed that in this situation, if both Δg and F_{ax} are expressed in p.u. values (i.e.: $\Delta g_{pu} = \Delta g / g_n$; $F_{ax.pu} = F_{ax} / F_{ref}$), the p.u. force equals the p.u. air gap variation, that is $F_{ax.pu} = \Delta g_{pu}$.
In [32], the reference force F_{ref} is the magnetic axial force developed in one air gap, due to the air gap flux density $B_g = \alpha_m \cdot B_m$:

$$F_{ref} = \frac{B_g^{\,2}}{2\cdot\mu_0}A_g \tag{13}$$

Therefore, we obtain

$$t_r(P_t) = \left\{\frac{3}{32\cdot E}\frac{(\alpha_m B_m)^2}{2\cdot\mu_0}\frac{\Delta g_{pu}}{k_{dr}g_n(P_t)}\frac{\left[D_e(P_t)\cdot(1-k_D)\right]^4}{1-\frac{\alpha_m B_m}{B_t}}\right\}^{\frac{1}{3}} \tag{14}$$

In this analysis, it is assumed Δg_{pu} = 0.2, k_{dr} = 0.1, E = 220,000 MPa (rays are made of C40 steel).

D. Other dimensions

Based on the sizing of the two prototypes, the following geometrical relations are assumed:

$$\begin{aligned} \ell_{ray}(P_t, N_{tcph}) &= \ell_m(P_t) + 2\cdot b_{ray}(P_t, N_{tcph}) \\ b_{rim}(P_t) &= 0.03\cdot D_e(P_t) \end{aligned} \tag{15-a}$$

$$\begin{aligned} \ell_{rim}(P_t, N_{tcph}) &= \frac{0.9\cdot k_D \cdot D_e(P_t)}{N_t(P_t, N_{tcph})} \\ \ell_{ci} &= 0.1\text{m (constant)} \\ \ell_{ce}(P_t) &= 0.1\cdot D_e(P_t) \\ A_c(P_t, N_{tcph}) &= 0.6\cdot b_{ray}(P_t, N_{tcph})^2 \end{aligned} \tag{15-b}$$

E. Reactance and resistances expressions .

The inductance $L_{p\ell}$ of the parasitic loop is in practice dependent on the permeance of the air gap facing two adjacent teeth. Thus, it can be expressed as $L_{p\ell} = \mu_0\cdot(2\cdot A_g/N_t) / g_e$, where g_e is the equivalent magnetic air gap $g_e = g_n + h_m /\mu_{rpu}$, and μ_{rpu} is the PM p.u. recoil permeability. Therefore, at the rated frequency f_n, the parasitic loop reactance $X_{p\ell n}$ is

$$X_{p\ell n}(P_t, N_{tcph}) = \frac{2\pi f_n(P_t)\cdot\mu_0\cdot 2\pi/4\, D_e(P_t)^2\left(1-k_D^{\,2}\right)}{N_t(P_t, N_{tcph})\left[g_n(P_t) + h_m(P_t)/\mu_{rpu}\right]} \tag{16}$$

Indicated with ρ_s the steel resistivity ($\rho_s = 1.5\cdot10^{-6}$ Ω·m), the resistances of the four branches of Fig. 6 are as follows:

$$\begin{aligned} R_{ray}(P_t, N_{tcph}) &= \rho_s \frac{\ell_{ray}(P_t, N_{tcph})}{b_{ray}(P_t, N_{tcph})\cdot t_r(P_t)} \\ R_{rim}(P_t, N_{tcph}) &= \rho_s \frac{0.5\cdot\ell_{rim}(P_t, N_{tcph})}{b_{rim}(P_t)\cdot t_r(P_t)} \\ R_{ce}(P_t, N_{tcph}) &= \rho_s \frac{\ell_{ce}(P_t, N_{tcph})}{A_c(P_t, N_{tcph})} \\ R_{ci}(P_t, N_{tcph}) &= \rho_s \frac{\ell_{ci}(P_t, N_{tcph})}{A_c(P_t, N_{tcph})} \quad . \end{aligned} \tag{17}$$

We remark that all the relations (1)-(15), which give the trend of the geometrical sizes with the power, are based on the prototypes sizing, but cannot match exactly the actual geometrical sizes of the prototypes; this implies that the reactance and resistances expressions (16)-(17) give different values, depending on which geometrical sizes are used, namely the sizes obtained by the model (1)-(15), or the prototypes actual sizes. Table IV reports the values of the parasitic loop reactance $X_{p\ell n}$ (at the rated frequency f_n) and of the branch resistances, evaluated in the two cases: the data labeled "model" are obtained by putting in (16)-(17) the geometrical sizes given by (1)-(15), whereas the data labeled "prototype" are obtained by putting in (16)-(17) the prototypes actual sizes. Note that the model and the prototype data are rather different each other, but the difference is not always in the same way: most times the model values are higher, but for R_{rim} the opposite occurs.

TABLE IV
PARASITIC LOOP REACTANCE (16) AND BRANCH RESISTANCES (17). COMPARISON BETWEEN THE VALUES GAINED BY USING THE SIZES OBTAINED BY THE MODEL (1)-(15) AND THE PROTOTYPE ACTUAL SIZES.

		resistances and reactance [μΩ]				
		R_{ray}	R_{rym}	R_{ce}	R_{ci}	$X_{p\ell n}$
50 kW	model (N_{tcph} = 6, P_t = 50 kW)	1024	52	141	134	365
	prototype	289	83	125	65	211
200 kW	model (N_{tcph} = 4, P_t = 200 kW)	736	20	172	91	428
	prototype	493	89	195	57	288

Fig. 8 shows graphically the trends of these quantities (eq.s (16)-(17), continuous lines) as a function of the machine power rating; also the prototype values are highlighted (markers). Only the results of the 200 kW prototype are shown, since the 50 kW case exhibits similar trends and level of agreement between model and prototype values.

In Fig. 8 and in some following trend analysis diagrams, discontinuities are introduced by *Round* functions used in equation (5) to force p and N_c to be integer numbers.

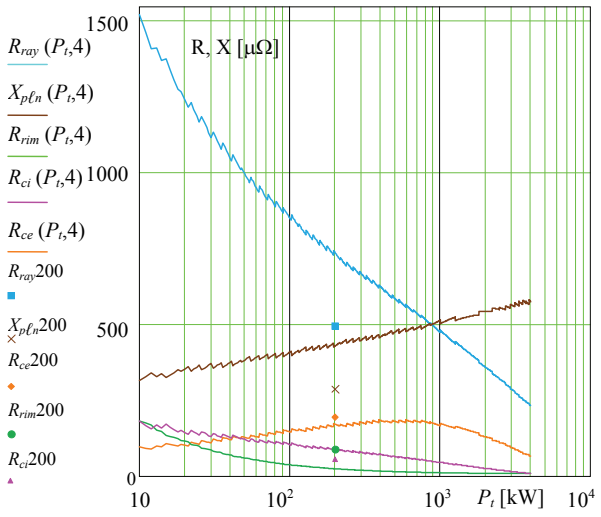

Fig. 8. Trends of the parasitic loop reactance and of the branch resistances (16)-(17) as a function of the machine power rating (continuous lines), together with the 200 kW prototype values (markers).

VI. Single Loop Parasitic Path Model

Fig. 9 shows the resistances which form the k-th couple (kA and kB) of the parasitic loops. In it, both the symbols of the loop inductance ($L_{p\ell}$) and of the EMF sources (e_{Ak} and e_{Bk}) do not appear, since they both cannot be attributed to a particular loop branch, but are related to the loop itself. The phasors of the loop currents $\bar{I}_{A.k}$ and $\bar{I}_{B.k}$ are also shown.

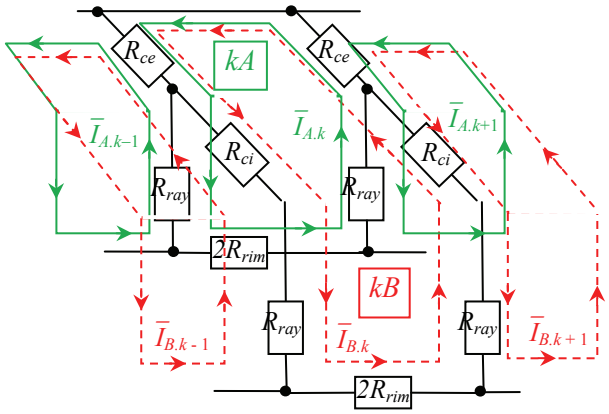

Fig. 9. Resistive elements of the k-th couple of parasitic loops shown in Fig. 6 (loops kA and kB) and phasors of the loop currents $\bar{I}_{A.k}$ and $\bar{I}_{B.k}$. The circuit symbols for inductances and EMFs are not drawn, because they cannot be attributed to particular branches, but to the loops only.

In the phasor domain, for the h-th harmonic (with $\omega_h = h\cdot\omega_n$), the voltage laws of the couple of loops are

$$\begin{aligned}\bar{E}_{Ak} &= -\left(R_{ce}+R_{ray}\right)\bar{I}_{A.k-1} - \left(R_{ce}+R_{ray}\right)\bar{I}_{A.k+1} + \\ &+2\left(R_{rim}+R_{ce}+R_{ray}+j\omega_h L_{p\ell}/2\right)\bar{I}_{A.k} + \\ &-R_{ce}\bar{I}_{B.k-1}+2R_{ce}\bar{I}_{B.k}-R_{ce}\bar{I}_{B.k+1}\end{aligned} \tag{18-a}$$

$$\begin{aligned}\bar{E}_{Bk} &= -\left(R_{ce}+R_{ray}+R_{ci}\right)\bar{I}_{B.k-1} - \left(R_{ce}+R_{ray}+R_{ci}\right)\bar{I}_{B.k+1} + \\ &2\left(R_{rim}+R_{ce}+R_{ray}+j\omega_h L_{p\ell}/2+2R_{ci}\right)\bar{I}_{B.k} + \\ &-R_{ce}\bar{I}_{A.k-1}+2R_{ce}\bar{I}_{A.k}-R_{ce}\bar{I}_{A.k+1}\end{aligned} \tag{18-b}$$

Parasitic loops form a meshed net; to solve it in a rigorous way, the equations of all the loops should be written, and the global system should be solved. Such an approach has been proposed in [30], [31]. Here, an approximated model is proposed, more suited for the general trend analysis here developed, because it is much simpler, being based on a single loop approach. As a matter of fact, the solution of the global system in [30], [31] showed that in a parasitic loop couple, the currents $\bar{I}_{A.k}$ and $\bar{I}_{B.k}$ are just slightly different each other: therefore, we consider only loops type A, and we assume $\bar{I}_{B.k} \approx \bar{I}_{A.k}$. Thus, (18-a) becomes

$$\begin{aligned}\bar{E}_{Ak} &= -\left(2R_{ce}+R_{ray}\right)\bar{I}_{A.k-1} - \left(2R_{ce}+R_{ray}\right)\bar{I}_{A.k+1} + \\ &+2\left(R_{rim}+2R_{ce}+R_{ray}+j\omega_h L_{p\ell}/2\right)\bar{I}_{A.k}\end{aligned} \tag{19}$$

The current phasors in the system of parasitic loops behave as the currents in the cage of an induction machine: they are all equal in magnitude, and the displacement between the current phasors of two adjacent loops is always the same. As regards the loop currents, the displacement angle equals twice the slot angle $\alpha_e = (2\pi/N_t)\cdot(p/2)$

$$\alpha_e(P_t, N_{tcph}) = \frac{2\pi}{N_t(P_t, N_{tcph})}\frac{p}{2} \tag{20}$$

Thus, the currents in the loops $k-1$ and $k+1$ can be expressed as

$$\bar{I}_{A.k-1} = \bar{I}_{A.k}\exp(j2\alpha_e) \qquad \bar{I}_{A.k+1} = \bar{I}_{A.k}\exp(-j2\alpha_e) \tag{21}$$

and (19) becomes $\bar{E}_{Ak} = \bar{Z}_{eq}\bar{I}_{A.k}$, where

$$\bar{Z}_{eq} = \left\{\begin{aligned}&2\left(R_{rim}+2R_{ce}+R_{ray}+j\omega_h L_{p\ell}/2\right)+\\&-\left(2R_{ce}+R_{ray}\right)\left[\exp(j2\alpha_e)+\exp(-j2\alpha_e)\right]\end{aligned}\right\} \tag{22}$$

The equivalent impedance (22) allows to obtain the loop current $\bar{I}_{A.k}$ very quickly; moreover, it has been verified that the error with respect to the solution of the global system in [30], [31] is very little (for the fundamental, lower than 0.1%).

By making explicit the functional dependencies, we have

$$\begin{aligned}\bar{Z}_{eq}(P_t, N_{tcph}, h) = 2&\left(\begin{aligned}&R_{rim}+2R_{ce}+R_{ray}+\\&j\omega_h(P_t,N_{tcph})L_{p\ell}(P_t,N_{tcph})/2\end{aligned}\right)+\\&-\left(2R_{ce}+R_{ray}\right)\left[\begin{aligned}&\exp(j2\alpha_e(P_t,N_{tcph}))+\\&+\exp(-j2\alpha_e(P_t,N_{tcph}))\end{aligned}\right]\end{aligned} \tag{23}$$

Similarly to Table IV, Table V reports the values of the equivalent impedance magnitude (for the fundamental component, i.e. h =1), evaluated when the geometrical sizes are obtained from the model (1)-(15) or are the actual sizes of the prototypes; in other words, (23) is evaluated by putting in it the data labeled "model" in Tab. IV, or the data labeled "prototype".

Fig. 10 shows graphically the trends of the impedance magnitude (continuous lines) with the machine power, together with the prototype values (markers). Again, the

discontinuities in the plots are due to the *Round* functions used in equation (5).

TABLE V
EQUIVALENT IMPEDANCE (22)-(23) MAGNITUDE [μΩ]
COMPARISON BETWEEN THE MODEL AND THE PROTOTYPE VALUES

50 kW	model	$\lvert \bar{Z}_{eq}(50e3,6,1) \rvert = 420$
	prototype	$\lvert \bar{Z}_{eq50} \rvert = 313$
200 kW	model	$\lvert \bar{Z}_{eq}(200e3,4,1) \rvert = 515$
	prototype	$\lvert \bar{Z}_{eq200} \rvert = 504$

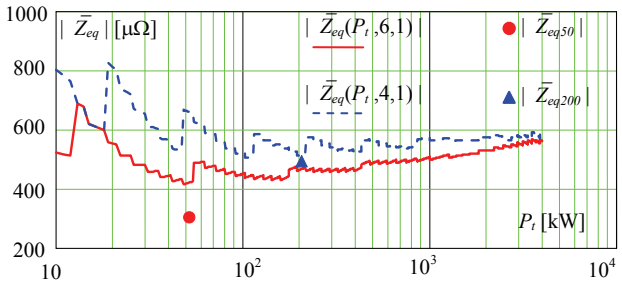

Fig. 10. Trend of the equivalent impedance Z_{eq} (22)-(23), as a function of the machine power (lines), together with the prototype values (markers).

Note that even if the model and the prototype resistances are rather different from each other (see values in Tab IV), the model and the prototype impedances are rather similar. This is due to the way how the several terms combine in (23) to give the equivalent impedance Z_{eq} , together with the fact that (as previously noted) the difference between the model and the prototype resistances is not always in the same way.

Thus, a perfect quantitative matching of prototype and model results for current and losses is not guaranteed. However, rather than an accurate evaluation of parasitic currents and losses, the aim of the model is the analysis of their general trend with the machine power and the understanding of scale effects. In addition, the precise computation of parasitic losses at the design stage needs accurate knowledge of steel resistivity and contact resistances at the interface between different elements included into parasitic loops. As known, resistivity in semi-finished steel products can undergo significant fluctuations, and modelling contact resistances accurately is highly challenging.

VII. EMFS AND PARASITIC CURRENTS EVALUATION

From [30], the rms value $E_{p\ell h}$ of the h-th harmonic of the parasitic loop EMF is expressed by

$$E_{p\ell h} = k_{th} \cdot 2 \cdot 2\pi h f_n \cdot \frac{\Phi_{th}}{\sqrt{2}} \tag{24}$$

where Φ_{th} is the h-th harmonic of the tooth flux (peak value of the phasor) and k_{th} is a composition factor of the fluxes of two adjacent teeth:

$$k_{th} = \left| cos\left(h \cdot \pi \cdot \frac{3 \cdot N_{tcph} + 1}{6 \cdot N_{tcph}} \right) \right|. \tag{25}$$

Another outcome of the analysis performed in [30] by means of the global system was that the contribution of the EMF harmonics to the parasitic currents is minor (about 7-8%). Thus, in order to have a quick and simple estimation of the parasitic current amount, only the fundamental parasitic loop EMF can be considered. Its rms value equals

$$E_{p\ell 1} = \left| sin\left(\frac{\pi}{6} \cdot \frac{1}{N_{tcph}} \right) \right| 2 \cdot 2\pi f_n \cdot \frac{\Phi_{t1}}{\sqrt{2}} \tag{26}$$

The fundamental Φ_{t1} of the tooth flux can be assumed equal to the peak value of the no-load tooth flux Φ_{tp}, occurring when the tooth axis is aligned to the PM axis [18]. It can be expressed [18] as

$$\Phi_{tp} = \frac{A_g}{p} \alpha_m B_m \tag{27}$$

By means of the relation $N_n = 120 \cdot f_n / p$, the rms value $E_{p\ell 1}$ of the fundamental of the parasitic loop EMF results

$$E_{p\ell 1}\left(P_t, N_{tcph}\right) = \left| sin\left(\frac{\pi}{6} \frac{1}{N_{tcph}} \right) \right| N_n\left(P_t\right) \frac{\pi}{30} \frac{\pi}{4\sqrt{2}} \alpha_m B_m \left(1 - k_D{}^2\right) D_e\left(P_t\right)^2 \tag{28}$$

Table VI reports the values of $E_{p\ell 1}$ (28) gained from the model (i.e., by using (1)-(2) for functions $N_n(P_t)$ and $D_e(P_t)$ in (28)) and from the prototypes (i.e., by using the values of N_n and D_e of the prototypes); Fig. 11 shows graphically the trends of $E_{p\ell 1}$ (continuous lines) with the machine power, together with the prototype values (markers).

TABLE VI
RMS OF THE FUNDAMENTAL OF THE PARASITIC LOOP EMF (28) [mV]
COMPARISON BETWEEN THE MODEL AND THE PROTOTYPE VALUES

50 kW	model	$E_{p\ell 1}(50e3,6) = 86$
	prototype	$E_{p\ell 1.50} = 81$
200 kW	model	$E_{p\ell 1}(200e3,4) = 265$
	prototype	$E_{p\ell 1.200} = 256$

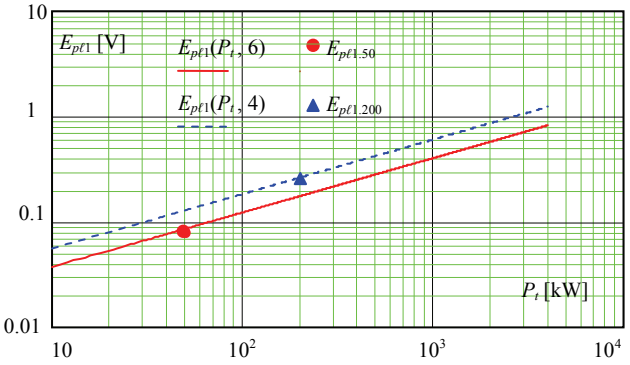

Fig. 11. Trend of the rms value of the fundamental EMF of the parasitic loop $E_{p\ell 1}$ (28), as a function of the machine power (continuous lines), together with the prototype values (markers).

Now, the currents in all the branches of the parasitic loops can be evaluated quickly. In particular, the magnitude of the rms fundamental current are evaluated as follows:

– the current $I_{loop.1}$ in one loop is given by:

$$I_{loop.1}\left(P_t, N_{tcph}\right) = \frac{E_{p\ell 1}\left(P_t, N_{tcph}\right)}{Z_{eq}\left(P_t, N_{tcph}, 1\right)} \quad ; \tag{29}$$

– the current $I_{ray.1}$ in one ray is given by the phasor composition of the currents of two adjacent loops:

$$I_{ray.1}\left(P_t, N_{tcph}\right) = 2\left|\sin\left(\alpha_e\left(P_t, N_{tcph}\right)\right)\right| I_{loop.1}\left(P_t, N_{tcph}\right) \quad ; \quad (30)$$

– the current $I_{cyl.1}$ in the external cylindrical spacer (object 5 in Figs. 4 and 6) is the sum of the currents in loops A and B (related to the same couple of teeth); since we assumed $\bar{I}_{B.k} = \bar{I}_{A.k}$, we obtain simply

$$I_{cyl.1}\left(P_t, N_{tcph}\right) = 2 I_{ray.1}\left(P_t, N_{tcph}\right). \quad (31)$$

Table VII reports the values of these three currents (29)-(31) from the model and from the prototypes. Tab. VII comes directly from Tab. V and VI: the model values of $I_{loop.1}$ in Tab. VII are obtained by using in (29) the model values of $E_{p\ell 1}$ and Z_{eq} reported in Tab. V and VI; in the same way, the prototypes values of $I_{loop.1}$ are obtained by using in (29) the prototype values of Tab. V and VI; $I_{ray.1}$ and $I_{cyl.1}$ derive from (30)-(31). Fig. 12 shows graphically the trend of $I_{cyl.1}$ (31) as a function of the machine power (lines), together with the prototype values (markers).

TABLE VII
MAGNITUDE OF THE RMS FUNDAMENTAL CURRENT (29)-(31) IN SOME BRANCHES OF THE PARASITIC LOOPS [Arms]
COMPARISON BETWEEN THE MODEL AND THE PROTOTYPE VALUES

		$I_{loop.1}$	$I_{ray.1}$	$I_{cyl.1}$
50 kW	model (N_{tcph} = 6, P_t = 50 kW)	205	58.5	117
	prototype	258	89.7	179
200 kW	model (N_{tcph} = 4, P_t = 200 kW)	513	246	491
	prototype	507	262	525

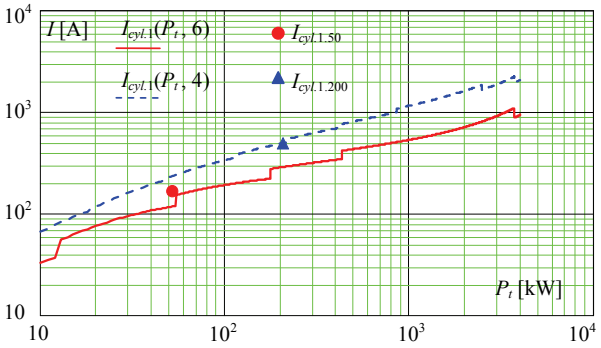

Fig. 12. Trend of the rms value of the fundamental currents in the external cylindrical spacers $I_{cyl.1}$ (31), as a function of the machine power (continuous lines), together with the prototype values (markers).

Figs. 10-12 show clearly that, as the power increases, the impedance of parasitic loops tends to become constant, whereas the EMF increases, thus the parasitic current increases too, and it can reach very high values (up to 1-2 kA for P_t in the MWs range). This suggests that with the power increase, the problem of the parasitic current becomes more critical, also in terms of corresponding losses and overheating. In particular, according to the single loop model in Fig. 9, Joule losses due to the fundamental components of parasitic currents can be estimated by (32):

$$P_{loss.1} = \frac{N_t}{2}\left[2 \cdot 2R_{rim} {I_{loop.1}}^2 + \left(2R_{ray} + R_{ci}\right) {I_{ray.1}}^2 + R_{ce} {I_{cyl.1}}^2\right] \quad (32)$$

All quantities in (32) depend on P_t and N_{tcph}. By substituting in (32) the expressions of the currents (29)-(31) and of the resistances (17), the expression of the function $P_{loss1}(P_t, N_{tcph})$ is gained. Fig. 13 shows the trends of P_{loss1} as a function of the machine power (lines), together with the prototype values (markers). The prototype values have been evaluated by substituting in (32) the prototype currents in Tab.VII and the prototype resistances in Tab IV.

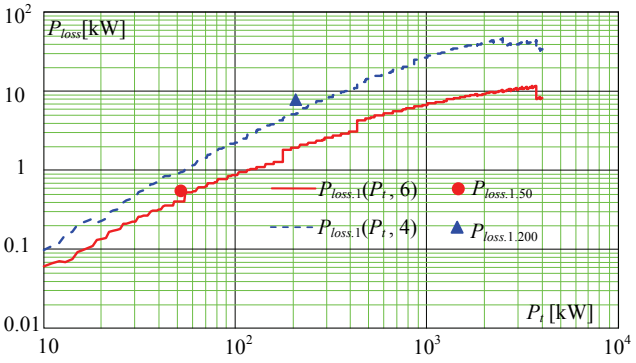

Fig. 13. Trend of the joule losses (due to the fundamental components of the parasitic currents) $P_{loss.1}$ (32), as a function of the machine power (continuous lines), together with the prototype values (markers).

Fig. 13 confirms the expectation about the losses due to the parasitic currents, and suggests that appropriate countermeasures have to be taken in order to open the parasitic loops. Being additional losses roughly independent of the delivered power, they are strongly detrimental for the efficiency at medium and low load: namely in the most usual operating conditions of a wind generator. Thus, the negative impact on the annual amount of energy production is expected to be significant.

The solution which will be tested in the next prototypes is the deposition of oxide layers on the rays surfaces in contact with the internal spacers (objects 6 in Figs. 4 and 6). In spite of its apparent simplicity, such a procedure involves some technological issues, mainly due to the extremely high contact stresses at the interface. Thus, special insulating layer materials with high resistance to wear should be selected, as wear may occur both during the machine assembly process and during operation, because of vibrations and additional stress at load.

VIII. CONCLUSION

This paper has analyzed the impact of scale effects on the circulation of parasitic currents in the stator frame structure of some YASA AFPM machines. A model has been developed to estimate the trend of the currents in the parasitic loops as a function of the machine power rating. The analysis has shown that as the power increases, the parasitic currents may increase very much, up to and over 1kA when the machine power reaches the MWs range. The trend of additional Joule losses produced by parasitic currents has also been evaluated. The detrimental effects of parasitic currents require the parasitic paths to be interrupted. The most promising solution seems the adoption of oxide layers, with high resistance to wear, to be placed in a few structural joints, in suited positions of the parasitic loops.

REFERENCES

[1] J.F. Gieras, Rong-Jie Wang, M.J. Kamper, "Axial Flux Permanent Magnet Brushless Machines," 2nd Edition, Springer, 2008.
[2] G. De Donato, F.G. Capponi, G. Borocci, F. Caricchi, L. Beneduce, L. Fratelli, A. Tarantino, "Ω-Shaped Axial-Flux Permanent-Magnet Machine for Direct-Drive Applications With Constrained Shaft Height," *IEEE Trans. Ind. App.*, vol.51, no.4, pp.3050-3058, July-

Aug. 2015.
[3] Fei Zhao, T.A. Lipo, Byung-il Kwon, "A Novel Dual-Stator Axial-Flux Spoke-Type Permanent Magnet Vernier Machine for Direct-Drive Applications," *IEEE Trans. Mag.*, vol.50, no.11, pp.1-4, Nov. 2014.
[4] W. Zhao, T.A. Lipo, B. Kwon, "A Novel Dual-Rotor, Axial Field, Fault-Tolerant Flux Switching Permanent Magnet Machine with High Torque Performance," *IEEE Trans. Mag.*, Early Access.
[5] Wenliang Zhao; T.A. Lipo, Byung-il Kwon, "Comparative Study on Novel Dual Stator Radial Flux and Axial Flux Permanent Magnet Motors With Ferrite Magnets for Traction Application," *IEEE Trans. Mag.*, vol.50, no.11, pp.1-4, Nov. 2014.
[6] O. Maloberti, R. Figueredo, C. Marchand, Y. Choua, D. Condamin, L. Kobylanski, E. Bomme, "3-D–2-D Dynamic Magnetic Modeling of an Axial Flux Permanent Magnet Motor With Soft Magnetic Composites for Hybrid Electric Vehicles," *IEEE Trans. Mag.*, vol.50, no.6, pp.1-11, June 2014.
[7] Yee-Pien Yang; Chung-Han Lee; Po-Chang Hung, "Multi-objective optimal design of an axial-flux permanent-magnet wheel motor for electric scooters," *IET Electric Power Applications*, vol.8, no.1, pp.1-12, January 2014.
[8] Yu-Seop Park; Seok-Myeong Jang; Ji-Hwan Choi; Jang-Young Choi; Dae-Joon You, "Characteristic Analysis on Axial Flux Permanent Magnet Synchronous Generator Considering Wind Turbine Characteristics According to Wind Speed for Small-Scale Power Application," *IEEE Trans. Mag.*, vol.48, no.11, pp.2937-2940, Nov. 2012.
[9] S. Djebarri, J.F. Charpentier, F. Scuiller, M. Benbouzid, "Design and Performance Analysis of Double Stator Axial Flux PM Generator for Rim Driven Marine Current Turbines," *IEEE Journal of Oceanic Engin.*, Early Access.
[10] S. Huang, T.A. Lipo, "Axial Flux Permanent Magnet Disc Machines: A Review," *International Symposium on Power Electronics, Electrical Drives, Automation, and Motion (SPEEDAM) 2004*, Capri, Italy, June 16-18, 2004.
[11] S. Kahourzade, A. Mahmoudi, Hew Wooi Ping; M.N. Uddin, "A Comprehensive Review of Axial-Flux Permanent-Magnet Machines," *Canadian Journal of Electrical and Computer Engineering,* , vol.37, no.1, pp.19-33, winter 2014.
[12] F. Giulii Capponi, G. De Donato, F. Caricchi, "Recent Advances in Axial-Flux Permanent-Magnet Machine Technology," *IEEE Trans. Ind. App.*, vol.48, no.6, pp.2190-2205, Nov.-Dec. 2012.
[13] F. Giulii Capponi, G. De Donato, A. Rivellini, F. Caricchi, "Fractional-Slot Concentrated-Winding Axial-Flux Permanent-Magnet Machine With Tooth-Wound Coils," *IEEE Trans. Ind. Appl.*, vol.50, no.4, pp.2446,2457, July-Aug. 2014.
[14] Sang-Ho Lee; Do-Jin Kim; Jung-Pyo Hong; Jun-Hong Park, "Characteristic Comparison Between the Spiral and the Lamination Stator in Axial Field Slotless Machines," *IEEE Trans. Mag.*, vol.45, no.10, pp.4547-4549, Oct. 2009.
[15] T.J. Woolmer, M.D. McCulloch, "Analysis of the Yokeless And Segmented Armature Machine," *IEEE International Conference on Electric Machines & Drives, IEMDC '07*, vol.1, pp.704-708, 3-5 May 2007.
[16] W. Fei, P. Luk, K. Jinupun, "A new axial flux permanent magnet Segmented-Armature-Torus machine for in-wheel direct drive applications," *IEEE Power Electronics Specialists Conference PESC 2008*, 15-19 June 2008, pp.2197-2202.
[17] H. Vansompel, P. Sergeant, L. Dupre, A. Van den Bossche, "Evaluation of a Simple Lamination Stacking Method for the Teeth of an Axial Flux Permanent-Magnet Synchronous Machine With Concentrated Stator Windings," *IEEE Trans. Mag.*, vol.48, no.2, pp.999-1002, Feb. 2012.
[18] A. Di Gerlando, G. M. Foglia, M. F. Iacchetti, R. Perini, "Axial Flux PM Machines With Concentrated Armature Windings: Design Analysis and Test Validation of Wind Energy Generators," *IEEE Trans. Ind. Electron.*, vol.58, no.9, pp.3795-3805, Sept. 2011.
[19] P. Sergeant, H. Vansompel, L. Dupre, "Performance and implementation issues considering the use of thin laminated steel sheets in segmented armature axial-flux PM machines," *Intern. Conf. on Electrical Machines (ICEM) 2014*, Berlin, 2-5 Sept. 2014, pp.1363-1369.
[20] H. Vansompel, P. Sergeant, L. Dupre, A. Van den Bossche, "Axial-Flux PM Machines With Variable Air Gap," *IEEE Trans. Ind. Electron.*, vol.61, no.2, pp.730-737, Feb. 2014.
[21] Takahiko Miura, Shinji Chino, Masatsugu Takemoto, Satoshi Ogasawara, Akira Chiba, Nobukazu Hoshi, "A Ferrite Permanent Magnet Axial Gap Motor with Segmented Rotor Structure for the Next Generation Hybrid Vehicle," *XIX Intern. Conf. on Electrical Machines - ICEM 2010*, Rome, ITALY, September 6-8, 2010, paper RF-014338.
[22] Bo Zhang, Yizhe Wang, M. Doppelbauer, M. Gregor, "Mechanical construction and analysis of an axial flux segmented armature torus machine," *Intern. Conf. on Electrical Machines (ICEM) 2014*, Berlin, 2-5 Sept. 2014, pp.1293-1299.
[23] H. Vansompel, P. Sergeant, L. Dupre, "Optimized Design Considering the Mass Influence of an Axial Flux Permanent-Magnet Synchronous Generator With Concentrated Pole Windings," *IEEE Trans. Mag.*, vol.46, no.12, pp.4101-4107, Dec. 2010.
[24] Electric Machine – Modular, by Nicholas Carpenter, Simon Dowson, Tim Woolmer, Chee Yeow Leong, William Treharne, Ma1colm McCulloch, (2011, Dec. 22), Patent Application PCT/GB2010/050236, Pub. No. US 2011/0309726 Al.
[25] Electric Machine - Over-Moulding Construction, by Tim Woolmer, Chris Gardner, Jon Barker, (2013, June 13), Patent Application PCT/GB2011/051550, Pub. No.: US 2013/0147291 A1.
[26] YASA Motors Products: http://www.yasamotors.com/products.
[27] J.G Wanjiku, H. Jagau, M.A. Khan, P. Barendse, "A simple core structure for small axial-flux PMSGs," *2011 IEEE International Electric Machines & Drives Conference (IEMDC)*, 15-18 May 2011, pp.1510-1515.
[28] A. Di Gerlando, G. Foglia, M. Iacchetti, R. Perini, "Design Criteria of Axial Flux PM Machines for Direct Drive Wind Energy Generation," *XIX Intern. Conf. on Electrical Machines ICEM 2010*, Rome, ITALY, September 6-8, 2010, Paper No RF-008168.
[29] A. Di Gerlando, G. M. Foglia, M. F. Iacchetti, R. Perini, "Analysis and Test of Diode Rectifiers Solutions in Grid Connected Wind Energy Conversion Systems Employing Modular Permanent Magnet Synchronous Generators," *IEEE Trans. Ind. Electron.*, vol. 59, no. 5, pp. 2135-2146, May 2012.
[30] A. Di Gerlando, G. M. Foglia, R. Perini, M. F. Iacchetti, "Analysis of stray paths for parasitic currents in some topologies of Yokeless and Segmented Armature Axial Flux PM Machines," *Intern. Conf. on Electrical Machines (ICEM) 2014*, Berlin, 2-5 Sept. 2014, pp.390-395.
[31] A. Di Gerlando, G. M. Foglia, R. Perini, M. F. Iacchetti, "Parasitic Currents in Structural Paths of YASA Axial Flux PM Machines: Estimation and Tests," *accepted for publication in IEEE Trans. Energy Conv.*
[32] A. Di Gerlando, G. M. Foglia, R. Perini, M. F. Iacchetti, "Effects of Manufacturing Imperfections in Concentrated Coil Axial Flux PM Machines: Evaluation and Tests," *IEEE Trans. Ind. Electron.*, Vol. 61, no. 9, pp. 5012-5024, Sept. 2014.

Antonino Di Gerlando (M'93) received his MS degree in electrical engineering from the Politecnico di Milano, Italy, in 1981. Currently, he is a Full Professor at the Department of Energy at Politecnico di Milano. Fields of interest: design and modeling of electrical machines, converters and drive systems. He is a member of IEEE, of the Italian Association of the Electric and Electronic Engineers (AEI), of the Electric Italian Committee of Standards (CEI) and of the SC of ICEM Conference.

Giovanni Maria Foglia received his MS degree and the PhD in electrical engineering at Politecnico di Milano, Milano, Italy, in 1997 and 2000.
Currently, he is an Assistant Professor at the Department of Energy at Politecnico di Milano, and his main field of interest is the analysis and design of PM electrical machines.

Matteo Felice Iacchetti (M'10) received the PhD in electrical engineering from the Politecnico di Milano, Milano, in 2008.
Currently, he is a Lecturer with the School of Electrical and Electronic Engineering at The University of Manchester, Manchester, UK. His main research interests are the design, modeling and control of electrical machines.

Roberto Perini (M'10) received his MS degree and the PhD in electrical engineering from the Politecnico di Milano, Milano, Italy.
Currently, he is an Associate Professor at the Department of Energy at Politecnico di Milano. His interests are in the design and modeling of electrical machines and wind energy conversion system.